



Simulation of glioblastoma growth using a 3D multispecies tumor model with mass effect

Shashank Subramanian¹ · Amir Gholami² · George Biros¹

Received: 17 October 2018 / Revised: 26 March 2019 / Published online: 24 May 2019
© Springer-Verlag GmbH Germany, part of Springer Nature 2019

Abstract

In this article, we present a multispecies reaction–advection–diffusion partial differential equation coupled with linear elasticity for modeling tumor growth. The model aims to capture the phenomenological features of glioblastoma multiforme observed in magnetic resonance imaging (MRI) scans. These include enhancing and necrotic tumor structures, brain edema and the so-called “mass effect”, a term-of-art that refers to the deformation of brain tissue due to the presence of the tumor. The multispecies model accounts for proliferating, invasive and necrotic tumor cells as well as a simple model for nutrition consumption and tumor-induced brain edema. The coupling of the model with linear elasticity equations with variable coefficients allows us to capture the mechanical deformations due to the tumor growth on surrounding tissues. We present the overall formulation along with a novel operator-splitting scheme with components that include linearly-implicit preconditioned elliptic solvers, and a semi-Lagrangian method for advection. We also present results showing simulated MRI images which highlight the capability of our method to capture the overall structure of glioblastomas in MRIs.

Keywords Glioma · Glioblastoma multiforme · Mass effect · Tumor growth · Multispecies · Linear elasticity

Mathematics Subject Classification 92C10 · 92C50 · 92C55 · 74L15 · 35K57

✉ Shashank Subramanian
shashanksubramanian@utexas.edu

Amir Gholami
amirgh@berkeley.edu

George Biros
biros@ices.utexas.edu

¹ Institute for Computational Engineering and Sciences, University of Texas at Austin, Austin, TX 78712, USA

² Department of Electrical Engineering and Computer Sciences, UC Berkeley, Berkeley, CA 94720, USA

1 Introduction

Glioblastomas form a class of highly aggressive tumors accounting for a majority of all malignant primary brain tumors in adults (Dolecek et al. 2012), with a median survival rate of 14.6 months (Stupp et al. 2005).

Mathematical modeling has been extensively used to assist in image analysis of MRIs (Gooya et al. 2011) as well as the diagnosis and treatment of brain tumors (Akbari et al. 2016; Hawkins-Daarud et al. 2013; Macyszyn et al. 2016; Szeto et al. 2009). There is a large body of work for generic tumor growth modeling at different scales and different scenarios (e.g., in vitro, animal models, multiscale models) that attempt to capture the complex biological principles underlying tumor dynamics by accounting for phenomena on cellular scales or continuum/tissue scales. In this paper, we are primarily interested in capturing the phenomenological features of glioblastomas observed from MRI scans. These include

- (i) enhancing rim of proliferating tumor cells,
- (ii) central tumor core filled with necrotic/dead cells,
- (iii) brain edema, and
- (iv) mass effect.

Our end goal is to couple this model with parameter estimation methods and with patient MRIs in order to assist in diagnosis and prognosis. The model also finds applications in areas like MR image segmentation of glioblastomas. For example, our model is incorporated in the training of neural networks on synthetic datasets as a data augmentation strategy in Gholami et al. (2018). Here, we only present the overall formulation.

A single species reaction–diffusion PDE has been one of the most popular modeling frameworks. This simple model attempts to capture two distinct behaviors of malignant tumor growth: proliferation (reaction) and infiltration (diffusion). However, it captures neither mass effect nor the characteristic imaging features of the visible tumor in MRI. Mass effect refers to the displacement of tissue cells due to tumor growth forces and is observed in both low grade and high-grade glioblastomas. Another distinct feature of glioblastomas is the presence of a proliferative/enhancing rim of tumor cells surrounding a central necrotic core. Moreover, imaging highlights regions of peritumoral edema. Edema typically surrounds the proliferative rim and is known to be dispersed with highly migratory tumor cells, called infiltrative or invasive tumor cells. These cells themselves are not visible in MRI scans. They invade healthy parenchyma to distances that measure several centimeters beyond the detectable tumor core (Giese et al. 2003). These cells are also able to invade in the presence of treatment and can escape surgical resections, leading to recurrence (Giese et al. 2003). An illustration of these imaging characteristics is shown in Fig. 1. MRI scans of patient brains with different ranges of mass effect are shown in Fig. 2.

Our hypothesis is that by designing a model that can capture these imaging characteristics (edema, enhancing and necrotic tumor, and mass effect), we will be able to extract clinically useful information. The model parameters can be inferred in a patient-specific manner and help improve the mathematical characterization of tumor, which ultimately betters the clinical outcome. In this paper, our goal is modest. We

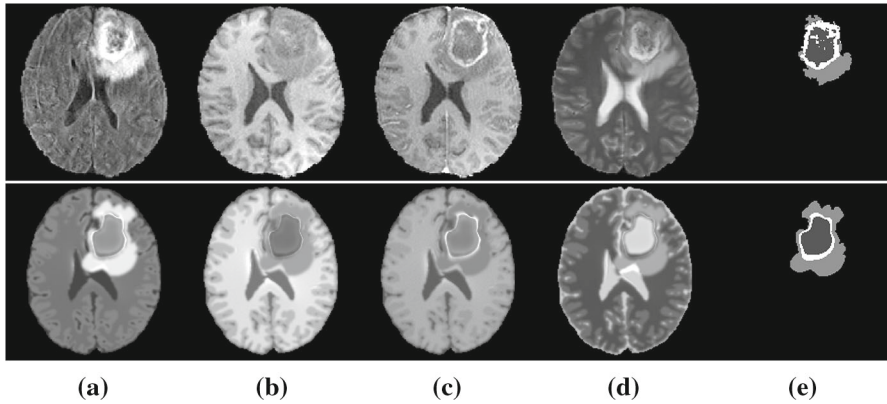


Fig. 1 Illustration of the phenomenological structures of a glioblastoma from MRI scans. All images are 2D slices of 3D volumetric datasets. (top row) These images correspond to a specific axial slice of **a** FLAIR, **b** T1, **c** T1-Gd, **d** T2 MRI, and **e** segmentation of a real patient brain, taken from the Multimodal Brain Tumor Segmentation Challenge, 2017 (Bakas et al. 2017b, a; Menze et al. 2015) training dataset. The peritumoral edema (light gray segmentation) is visible in the hyper-intense signal in the FLAIR image, while the enhancing tumor structures (white segmentation) and necrotic tumor core (dark gray segmentation) are visible in the T1-Gd MRI scan. We can also observe a noticeable amount of mass effect. (bottom row) Simulated MRI modalities from our current multispecies model with mass effect. These are generated by growing a synthetic tumor *in silico* using a healthy brain image. Once we solve our model, we create images by using correlations between tissue type and MRI intensity obtained by existing segmentations. We use the scans (and their corresponding segmentations) from the GLISTR dataset (Gooya et al. 2012) to achieve this. As one can see, the simulation captures many of the important features present in a real MR image

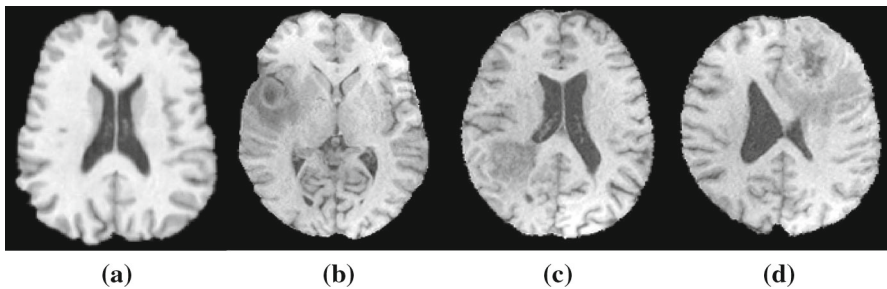


Fig. 2 T1 MRI scans of **a** a healthy brain, **b** brain with negligible mass effect, **c** moderate mass effect, and **d** significant mass effect

introduce a possible model that integrates the structure of a glioblastoma with its mechanical effects on surrounding brain tissue. Multispecies models are useful in this context as they help in delineating the different tumor regions effectively without ad-hoc thresholding operations which one might have to use when working with single species models. However, we also want to emphasize that we tried to design a model that is as *simple* as possible so it can be used in a robust way for parameter estimation. Indeed, highly complex and first principle models include many more tumor species, angiogenesis, chemotaxis, porous media that capture the interstitial fluid and extracellular matrix, and sophisticated models of growth. However, such models have a

large number of unknown parameters and pose outstanding numerical challenges with respect to both simulation and parameter estimation. Following the ideas in Yankeelov et al. (2013), our goal here is to introduce a *minimal* model that serves our clinical objective.

Related work: The most widely used tumor-growth model is the single species reaction–diffusion model, owing to its simplicity (Clatz et al. 2005; Hogeia et al. 2007; Jbabdi et al. 2005; Konukoglu et al. 2010b; Mang et al. 2012; Rekik et al. 2013; Swanson et al. 2000, 2002). But tumors are very complex with a multitude of underlying biological processes. These include mitosis, invasion, angiogenesis, biomechanics, environment quality, genotype, and gene expression. Approaches span from modeling each tumor phenotype on a cellular level (Alarcón et al. 2003; Anderson et al. 2009; Gerlee and Anderson 2009) to macroscopic descriptions of tumor densities and nutrient supply (Bellomo et al. 2008; Hawkins-Daarud et al. 2013; Konukoglu et al. 2010a, b; Oden et al. 2013; Swanson 2008; Swanson et al. 2011). Some of the simplest multispecies models are based on the “go-or-grow” hypothesis for differentiation. This hypothesis stems from experimental evidence (Giese et al. 1996, 2003) that suggests the existence of tumor cells in different interchangeable states based on the nutritional condition of their environment (Hatzikirou et al. 2012). While some models conform to the “go-or-grow” hypothesis (Pham et al. 2012; Saut et al. 2014), others do not consider this phenotype. Swanson et al. (2011) stipulate the existence of normoxic and hypoxic tumor cells which migrate at the same rate. These are complex multispecies models but they do not include mass effect, which is important for both low and high-grade glioblastomas.

Although tumor models date to the 1950s, models with mass effect are more recent. Early models (Hogeia et al. 2006; Mohamed and Davatzikos 2005) decoupled mass effect from tumor growth. The brain was modeled as an elastic material with external forces controlling the size of the tumor and displacements of surrounding tissue. More recent models, specifically the ones introduced in Hogeia et al. (2007), Hormuth et al. (2018) and Rahman et al. (2017), couple tumor dynamics with elasticity equations. These models show flexibility in capturing complex/realistic tumor shapes and associated mass effect. These models, however, only deal with a single species of tumor cells.

Contributions: In this paper, we propose a new model for glioblastoma growth dynamics, a novel numerical scheme, and we present exemplary results. In particular:

1. We propose a new go-or-grow, multispecies model coupled with an elasticity model for mass effect (Sect. 2). We model proliferative cells, invasive cells, necrotic cells and oxygen concentration. We use a new, mass-conserving formulation that excludes the cerebrospinal fluid (which is not mass-conserved in the MR-defined control volume we use). In addition, we introduce a *screened* elasticity model that can better localize mass effect.
2. We propose and test novel numerical schemes to discretize and solve the resulting model PDEs (Sect. 3). Introducing a two-way coupling between the tumor evolution equations and linear elasticity results in challenging numerical problems as it leads to time dependence of various material and tumor properties. This is because the brain geometry changes as the tumor grows (due to the mass effect). Further,

solving the linear elasticity equations is computationally challenging. The elasticity operator contains time and space varying coefficients and the non-linearity of the tumor growth model adds to the numerical challenges. The numerical schemes used in our solver include stable pseudo-spectral methods, a semi-Lagrangian scheme for transport equations and preconditioners for the variable elasticity and diffusion equations.

3. In the results section Sect. 4, we compare our model with a single species model with and without mass effect. We perform sensitivity analysis of our model parameters and finally present synthetic MR images highlighting the characteristic features of a glioblastoma.

Our model is inspired by Hoge et al. (2007) for the elasticity model and Saut et al. (2014) for the multispecies model. We detail the differences of our model with these two models in Sect. 2.

Limitations: Phenomenological models can account for a wide range of complex phenomena. An important phenomenon is angiogenesis, which can be measured with perfusion MRI data. We do not include angiogenesis as we wanted to minimize the number of unknown parameters to the extent possible. Another phenomenon is possible anisotropic diffusion of the tumor, which can be modeled if Diffusion Tensor Imaging (DTI) data is available (Painter and Hillen 2013; Swan et al. 2018). Even without angiogenesis or anisotropy our model has a large number of parameters, many of which are patient specific. This is related to the second limitation, which is lack of validation. One way to validate our model is to infer model parameters from actual patients and examine the mismatch between our model predictions and real patient data (see Gholami et al. (2016) for inverse tumor problem formulations with single species reaction–diffusion models). The model we present here is much more complicated and the latter approach is the focus of our immediate future work.

2 Forward tumor mathematical model

In the following subsections, we first introduce the screened elasticity model for mass effect, second we introduce the mass-conserving single species model with elasticity coupling and finally, the overall multispecies model. We also use the single species model for comparisons with our multispecies model.

2.1 Elasticity model

We model the displacement (\mathbf{u}) due to tumor-induced mass effect using linear elasticity. The governing equations of linear elasticity for an isotropic medium are given by:

$$\mathbf{T} = \lambda \text{tr}(\mathbf{E})\mathbf{I} + 2\mu\mathbf{E}, \quad (1a)$$

$$\nabla \cdot (\mu(\nabla\mathbf{u} + \nabla\mathbf{u}^T)) + \nabla(\lambda\nabla \cdot \mathbf{u}) + \mathbf{b} = \mathbf{0} \quad \text{in } \Omega, \quad (1b)$$

where \mathbf{T} is the stress tensor, \mathbf{E} is the infinitesimal strain tensor, (λ, μ) are Lamé coefficients and \mathbf{b} is the total body force. In order to prevent excessive shear to limit far

field effects of the resulting force, our model supports the screening of the elasticity equation with a screening coefficient, $\eta(\mathbf{x}, t)$, which will be a function of tumor concentration. We take η to be zero in the presence of tumor cells, and a high value elsewhere to screen the effects of the tumor. We show examples of the effects of screening in Sect. 4. We write the screened elasticity equation in a more compact form as:

$$-\eta \mathbf{u} + \mathcal{L} \mathbf{u} = \mathbf{b} \quad \text{in } \Omega, \tag{2}$$

where \mathcal{L} denotes the linear elasticity operator. The screening coefficient η can be varied to obtain different mass effect ranges and subsequent deformations of the material properties. The Lamé coefficients $(\lambda(\mathbf{x}, t), \mu(\mathbf{x}, t))$ are computed as:

$$\mu = \sum_s \frac{E_s}{2(1 + \nu_s)} \iota_s \tag{3a}$$

$$\lambda = \sum_s \frac{\nu_s E_s}{(1 - 2\nu_s)(1 + \nu_s)} \iota_s. \tag{3b}$$

Here, $\iota_s(\mathbf{x}, t)$ is the concentration of the constituent species s (tumor and healthy cells), E_s is the Young’s modulus of the species s and ν_s is Poisson’s ratio of the species s .

2.2 Reaction–diffusion model coupled with linear elasticity

The single species tumor model consists of a conservation equation with reaction and diffusion source terms for the evolution of the tumor cell concentration, $c(\mathbf{x}, t)$, and is coupled with the linear elasticity equation (Eq. 2). The model can be summarized by the following equations:

$$\partial_t c + \nabla \cdot (c \mathbf{u}_t) - \mathcal{D}c - \mathcal{R} = 0 \quad \text{in } \Omega \times (0, 1] \tag{4a}$$

$$c_0 - \Phi \mathbf{p} = 0 \quad \text{in } \Omega \tag{4b}$$

$$-\eta \mathbf{u} + \mathcal{L} \mathbf{u} - \mathbf{b} = 0 \quad \text{in } \Omega \times (0, 1] \tag{4c}$$

$$\partial_t g + \nabla \cdot (g \mathbf{u}_t) + \frac{g}{g + w} (\mathcal{D}c + \mathcal{R}) = 0 \quad \text{in } \Omega \times (0, 1] \tag{4d}$$

$$\partial_t w + \nabla \cdot (w \mathbf{u}_t) + \frac{w}{g + w} (\mathcal{D}c + \mathcal{R}) = 0 \quad \text{in } \Omega \times (0, 1] \tag{4e}$$

$$\partial_t f + \nabla f \cdot \mathbf{u}_t = 0 \quad \text{in } \Omega \times (0, 1] \tag{4f}$$

$$g - g_0 = 0 \quad \text{in } \Omega \tag{4g}$$

$$w - w_0 = 0 \quad \text{in } \Omega \tag{4h}$$

$$f - f_0 = 0 \quad \text{in } \Omega. \tag{4i}$$

The basic model notation is described in Table 1. We briefly explain the individual components of the model below.

Our goal is to be able to decide the properties of a voxel in order to create a segmentation that we can compare with MRI imaging data. Therefore, we introduce

Table 1 Common notations for the reaction–diffusion tumor model

| Notation | Description |
|--|---|
| $c(\mathbf{x}, t)$ | Tumor concentration |
| $g(\mathbf{x}, t)$ | Gray matter concentration |
| $w(\mathbf{x}, t)$ | White matter concentration |
| $f(\mathbf{x}, t)$ | Cerebrospinal fluid density |
| $(c_0(\mathbf{x}), g_0(\mathbf{x}), w_0(\mathbf{x}), f_0(\mathbf{x}))$ | Initial conditions for corresponding cell densities |
| $\mathbf{u}_r(\mathbf{x}, t)$ | Advection velocity |
| $\mathbf{b}(\mathbf{x}, t)$ | Linear elasticity forcing function |
| \mathcal{D} (see Eq. 7) | Diffusion operator |
| \mathcal{R} (see Eq. 9) | Reaction operator |
| $\mathbf{x} = (x, y, z)$ | Spatial location |
| t | Time |
| Ω | Spatial domain |
| Φ | Gaussian basis functions for tumor initial condition parameterization |
| $\mathbf{p} \in \mathbb{R}^{N_p}$ | Tumor initial condition parameterization |

the following assumption: the total cell density is mass-conserved (similar to the assumptions introduced in Saut et al. 2014). We define the total cell density as a sum of all component densities, i.e:

$$c + g + w = m, \quad (5)$$

where m is the total cell density, which we assume is conserved. It thus satisfies:

$$\partial_t m + \nabla \cdot (m \mathbf{u}_t) = 0 \quad \text{in } \Omega \times (0, 1]. \quad (6)$$

Then the conservation laws for the healthy cells, Eqs. 4d and 4e, follow from Eq. 6. We note that the cerebrospinal fluid is not included. We apply a pure advection equation (Eq. 4f) to the cerebrospinal fluid to account for possible leakage. This approach differs from the one in Hogeia et al. (2007), where the evolution of material properties is not in conservative form and does not account for the loss of healthy cells through tumor growth and invasion.

The differential operator \mathcal{D} is the inhomogeneous isotropic diffusion operator:

$$\mathcal{D}c = \nabla \cdot (\mathbf{K}(g(\mathbf{x}, t), w(\mathbf{x}, t), f(\mathbf{x}, t), \mathbf{x}) \nabla c). \quad (7)$$

The diffusion coefficient \mathbf{K} is given by:

$$\mathbf{K}(g(\mathbf{x}, t), w(\mathbf{x}, t), \mathbf{x}) = k_g g(\mathbf{x}, t) \mathbf{I} + k_w w(\mathbf{x}, t) \mathbf{I}, \quad (8)$$

where k_g and k_w are the constant diffusion rates in gray and white matter, respectively. The reaction operator is a non-linear logistic growth function:

$$\mathcal{R} = \rho(\mathbf{x}, t)c(1 - c), \quad (9)$$

where

$$\rho(\mathbf{x}, t) = \rho_g g(\mathbf{x}, t) + \rho_w w(\mathbf{x}, t). \quad (10)$$

Here, ρ_g and ρ_w are constant growth rates in gray and white matter, respectively. Note that the diffusion and reaction operators now depend on the material properties that change in time. This is due to the evolution of the tumor growth, which in turn displaces the surrounding tissue.

The forcing function for the linear elasticity equations is modeled as

$$\mathbf{b} = \zeta \tanh(c) \nabla c, \quad (11)$$

where ζ is a constant. The choice of the force function is not unique and other formulations are possible as well (Hogea et al. 2008). Here, we assume that the force exerted on the brain tissue is proportional to the tumor concentration gradient. The addition of the $\tanh(c)$ term is to enforce small displacement forces where the tumor concentration is small. More complex models like poroelasticity or growth models (Gorieli and Moulton 2011) which change the constitutive equation and write the deformation gradient as a product of an elastic and growth term can be used, but these are highly nonlinear and with a large number of unknown parameters. Since here we are not developing a first-principles model but instead a more phenomenological model to be used in conjunction with imaging information, we use the simple linear elasticity model of Sect. 2.1.

Regarding boundary conditions, we assume zero tumor flux on the skull and cerebrospinal fluid boundaries and zero displacement on the skull. The Lamé coefficients are different depending on the tissue type (tumor, gray matter, white matter, cerebrospinal fluid). In our model (both single and multi-species), we assume that the healthy tissues of the brain are slightly compressible and the tumorous tissues are nearly incompressible with a Young's modulus similar to that of healthy tissues. The cerebrospinal fluid is modeled as a highly compressible and soft material. The different model parameters used for our simulations are highlighted in Table 3.

2.3 Multispecies model coupled with linear elasticity

We modify the model introduced by Saut et al. (2014) and couple it with linear elasticity equations to capture mass effect. The basic structure of Saut et al. (2014) assumes active tumor cells to exist in either one of two states, proliferative and invasive. If the tumor microenvironment has sufficient concentration of oxygen and other nutrients, the tumor cells grow through rapid mitosis by consuming those nutrients. If the oxygen concentration becomes low (hypoxia), the cells switch from proliferative to invasive.

Invasive cells migrate to surrounding areas with higher nutrition concentration and switch back to proliferating cells when such an environment becomes available. This model assumes the only significant environmental factor affecting the state of tumor cells to be oxygen. In the event of severe hypoxia, the tumor cells die and become necrotic, typically located in the center of the tumor. The model is given by the following set of partial differential equations:

$$\partial_t p + \nabla \cdot (p \mathbf{u}_t) - \mathcal{R} + \alpha p - \beta i + hp = 0 \quad \text{in } \Omega \times (0, 1] \quad (12a)$$

$$p_0 - \Phi \mathbf{p} = 0 \quad \text{in } \Omega \quad (12b)$$

$$\partial_t i + \nabla \cdot (i \mathbf{u}_t) - \mathcal{D}i - \tilde{\mathcal{R}} + \beta i - \alpha p + hi = 0 \quad \text{in } \Omega \times (0, 1] \quad (12c)$$

$$i_0 - \Phi \tilde{\mathbf{p}} = 0 \quad \text{in } \Omega \quad (12d)$$

$$\partial_t n + \nabla \cdot (n \mathbf{u}_t) - hp - hi - h(g + w) = 0 \quad \text{in } \Omega \times (0, 1] \quad (12e)$$

$$n_0 = 0 \quad \text{in } \Omega \quad (12f)$$

$$\partial_t o - \mathcal{D}o + \delta_p p - \delta_s (o_{\text{heal}} - o)(g + w) = 0 \quad \text{in } \Omega \times (0, 1] \quad (12g)$$

$$o_0 - o_{\text{heal}} = 0 \quad \text{in } \Omega \quad (12h)$$

$$-\eta \mathbf{u} + \mathcal{L} \mathbf{u} - \mathbf{b} = 0 \quad \text{in } \Omega \times (0, 1] \quad (12i)$$

$$\partial_t g + \nabla \cdot (g \mathbf{u}_t) + \frac{g}{g + w} (\mathcal{D} + \mathcal{R} + \tilde{\mathcal{R}}) + hg = 0 \quad \text{in } \Omega \times (0, 1] \quad (12j)$$

$$\partial_t w + \nabla \cdot (w \mathbf{u}_t) + \frac{w}{g + w} (\mathcal{D} + \mathcal{R} + \tilde{\mathcal{R}}) + hw = 0 \quad \text{in } \Omega \times (0, 1] \quad (12k)$$

$$\partial_t f + \nabla f \cdot \mathbf{u}_t = 0 \quad \text{in } \Omega \times (0, 1] \quad (12l)$$

$$g - g_0 = 0 \quad \text{in } \Omega \quad (12m)$$

$$w - w_0 = 0 \quad \text{in } \Omega \quad (12n)$$

$$f - f_0 = 0 \quad \text{in } \Omega. \quad (12o)$$

The common notations used in the multispecies model are outlined in Table 2. We provide a brief description of the details of the model below.

The governing equation for proliferative cells is a conservation equation with the following source terms: reaction corresponding to cell mitosis in favorable environments, phenotype switches between proliferative and invasive based on the quality of the environment, and a death term in hypoxic regions. The evolution of invasive cells is governed by a diffusion equation with source terms representing similar behavior as proliferative cells. The conservation equation for necrotic cells is primarily driven by sources corresponding to the death of tumorous and healthy cells in hypoxic environments.

Ignoring cerebrospinal fluid, we define the total cell density as:

$$p + i + n + g + w = m. \quad (13)$$

The conservation laws for the healthy cells follow from the mass conservation of the total cell density (similar to the single species model). We use a pure advection equation to model the evolution of the cerebrospinal fluid.

Table 2 Common notations for the multispecies go-or-grow tumor model

| Notation | Description |
|--------------------------------------|--|
| $p(\mathbf{x}, t)$ | Proliferative tumor cell concentration |
| $i(\mathbf{x}, t)$ | Invasive tumor cell concentration |
| $n(\mathbf{x}, t)$ | Necrotic tumor cell concentration |
| $o(\mathbf{x}, t)$ | Oxygen concentration |
| o_{heal} | Healthy cell oxygen concentration |
| $\alpha(\mathbf{x}, t)$ (see Eq. 17) | Transition rate from p to i cells |
| $\beta(\mathbf{x}, t)$ (see Eq. 18) | Transition rate from i to p cells |
| $h(\mathbf{x}, t)$ (see Eq. 14) | Oxygen threshold function |
| \mathcal{R} (see Eq. 15) | Proliferative cell reaction operator |
| $\tilde{\mathcal{R}}$ (see Eq. 16) | Invasive cell reaction operator |
| δ_p | Oxygen consumption rate |
| δ_s | Oxygen supply rate |

We use a thresholding function h based on the concentration of oxygen to model the death of cancer and healthy cells through a death rate γ :

$$h = \gamma \mathcal{H}(o_{\text{hypoxia}} - o), \tag{14}$$

where o_{hypoxia} is the hypoxia threshold and \mathcal{H} is a smoothed Heaviside function. We model the reaction operator for the proliferative cells \mathcal{R} as:

$$\mathcal{R} = \begin{cases} \rho p(1 - p), & o > o_{\text{inv}} \\ \left(\frac{o - o_{\text{mit}}}{o_{\text{inv}} - o_{\text{mit}}}\right) \rho p(1 - p), & o_{\text{inv}} \geq o \geq o_{\text{mit}} \\ 0, & o < o_{\text{mit}}, \end{cases} \tag{15}$$

where o_{mit} and o_{inv} are mitosis and invasive oxygen thresholds, respectively. We use $o_{\text{mit}} = (o_{\text{hypoxia}} + o_{\text{inv}})/2$. Here, $\rho = \rho(\mathbf{x}, t)$ is the proliferation rate as defined in Eq. 9. For invasive cells, the reaction operator $\tilde{\mathcal{R}}$ is similarly defined as

$$\tilde{\mathcal{R}} = \begin{cases} \rho i(1 - i), & o > o_{\text{inv}} \\ \left(\frac{o - o_{\text{mit}}}{o_{\text{inv}} - o_{\text{mit}}}\right) \rho i(1 - i), & o_{\text{inv}} \geq o \geq o_{\text{mit}} \\ 0, & o < o_{\text{mit}}. \end{cases} \tag{16}$$

We assume that invasive cells proliferate at a much smaller rate compared to proliferative cells. We take ρ_w^i , the proliferation rate of invasive cells in white matter as a small fraction of ρ_w (see Eq. 9). We model the transition rate α as a decreasing function of oxygen concentration by the expression:

$$\alpha = \alpha_0 \mathcal{H}(o_{\text{inv}} - o). \quad (17)$$

The transition rate β is modeled as:

$$\beta = \beta_0 (\mathcal{H}(\sigma_b - p - i) o), \quad (18)$$

where σ_b is a threshold above which the transition to p is prohibited. The rate is an increasing function of oxygen concentration to prevent cells from converting to the proliferative phenotype in scarcity of oxygen.

The evolution of oxygen is modeled through a diffusion equation. The source of oxygen is assumed to be proportional to the concentration of healthy cells and oxygen is consumed by proliferation at a constant rate δ_p .

We use

$$\mathbf{b} = \zeta \tanh(p + n) \nabla(p + n) \quad (19)$$

for the forcing function of the linear elasticity, similar to the single-species model.

2.4 Tumor-associated brain edema model

Cerebral edema in glioblastomas arise primarily from the leakage of protein and fluid into the extra-cellular matrix of the brain. Edema is a prominent image phenotype of glioblastomas, since it is clearly visible in MR images and is typically infiltrated by invasive tumor cells that lead to post-resection recurrence. The mechanism of fluid accumulation due to the tumor is often modeled as a consequence of the infiltrative property of tumor cells. We choose a model based on the works of Hawkins-Daarud et al. (2013). The infiltrative tumor cells cause the fluid to leak into the extra-cellular space, where it moves through diffusion. A constant drainage term models the re-absorption of fluid into the vascular system. The equations governing the evolution of edema are one-way coupled to the multispecies tumor growth model and are given below:

$$l_t = \mathcal{D}l + \delta_e \frac{i}{i + \delta_{\text{half}}} (1 - i) - \delta_l l, \quad (20)$$

where l is the edematous fluid concentration, δ_e is a measure of the transmission rate of edema into the extra-cellular space, δ_{half} is the concentration of invasive cells at which δ_e reaches half of its maximum value and δ_l is the rate of drainage of edema back into the system. We note that this model is de-coupled from the linear elasticity equations. We assume that the stress due to fluid leakage is insignificant in comparison to the stress induced through tumor growth. However, even this simplistic model will have important consequences for a parameter estimation problem since any unrealistic model coefficients will be unable to reproduce the observed edema. Hence, as a first step, we have settled for this model. We note that the nature of edematous fluid from MRI images can also be approximated by:

$$l = (1 - p - i - n)\mathcal{H}(i - i_{\text{threshold}}), \quad (21)$$

with some threshold value chosen for invasive cells, $i_{\text{threshold}}$.

2.5 Model parameters

The multi-species model presented above has 27 parameters (essentially material properties). Approximate (range of) values are given for some of these parameters in literature and we use similar values. The values for the various model parameters are summarized in Table 3. In particular, we refer to Gholami et al. (2016) for reaction and diffusion coefficient values, Saut et al. (2014) for the multispecies model parameter values, Hoge et al. (2007) for the elasticity model parameter values and Hawkins-Daarud et al. (2013) for the edema model parameter values. For screening coefficient values and edema model parameter values, we experiment with different values to produce reasonable qualitative characteristics of mass effect and edema in MRI images.

3 Discretization and numerical scheme

We use the fractional operator splitting method (Strang 1968) in conjunction with pseudo-spectral methods to numerically solve the non-linear system of PDEs. All spatial derivatives are computed using the fast Fourier transform (FFT). First, we describe the discretization scheme for the single species model outlined in Eq. 4. Then, we describe the discretization for the multispecies model.

We use a fictitious domain method where the brain is assumed to reside in a cubic box. The space is discretized uniformly into 256^3 nodes with spatial resolution $1\text{ mm} \times 1\text{ mm} \times 1\text{ mm}$.

Given tumor concentration c^n at time step n , healthy tissue concentrations (g^n, w^n, f^n), and corresponding material-dependent reaction and diffusion coefficients, we solve the single species model (Eq. 4) through the following operator splitting steps:

- Solve the advection equations $\partial_t q + \nabla \cdot (q \mathbf{u}_t) = 0$ for $q = (c, g, w)$ over time Δt using the semi-Lagrangian method (see Falcone and Ferretti 1998; Mang et al. 2016), with (c^n, g^n, w^n) as initial condition and current velocity \mathbf{u}_t^n to obtain $(c^\dagger, g^\dagger, w^\dagger)$.
- Solve the advection equation $\partial_t f + \nabla f \cdot \mathbf{u}_t = 0$ for f over time Δt using the semi-Lagrangian method with f^n as initial condition and current velocity \mathbf{u}_t^n to obtain f^{n+1} .
- Solve the diffusion equation $\partial_t c - \mathcal{D}c = 0$ over time Δt using the Crank-Nicolson method (Crank and Nicolson 1996) with c^\dagger as initial condition to obtain $c^{\dagger\dagger}$.
- Solve the reaction equations $\partial_t q - \mathcal{R}_q = 0$ over time Δt explicitly with $(c^{\dagger\dagger}, g^\dagger, w^\dagger)$ as initial condition to obtain $(c^{n+1}, g^{n+1}, w^{n+1})$. Here, \mathcal{R}_q is the reaction/source operator for Eqs. 4a, 4d and 4e. Update the reaction, diffusion and elasticity coefficients using the new healthy tissue and tumor concentration.

Table 3 Model parameters used in the forward simulations

| Parameter | Value |
|---|--------|
| <i>Reaction and diffusion coefficients</i> (see Gholami et al. 2016) | |
| Diffusion coefficient in white matter, k_w (see Eq. 8) | 0.1 |
| Diffusion coefficient in gray matter, k_g (see Eq. 8) | 0 |
| Reaction coefficient in white matter, ρ_w (see Eq. 10) | 8 |
| Reaction coefficient in gray matter, ρ_g (see Eq. 10) | 0 |
| Reaction coefficient of invasive cells in white matter, ρ_w^i (see Eq. 16) | 0.8 |
| <i>Go-or-grow model parameters</i> (see Saut et al. 2014) | |
| Transition rate coefficient from p to i , α_0 (see Eq. 17) | 0.15 |
| Transition rate coefficient from i to p , β_0 (see Eq. 18) | 0.02 |
| Death rate, γ (see Eq. 14) | 1 |
| Transition threshold from i to p , σ_b (see Eq. 18) | 0.9 |
| Hypoxia oxygen threshold, o_{hypoxia} (see Eq. 14) | 0.65 |
| Invasive oxygen threshold, o_{inv} (see Eq. 15) | 0.7 |
| Oxygen supply, δ_s (see Eq. 12g) | 55 |
| Oxygen consumption rate, δ_p (see Eq. 12g) | 8 |
| <i>Screening parameters</i> | |
| Screening factor in tumor cells, η_{tumor} (see Eq. 2) | 0 |
| Screening factor in healthy cells, $\eta_{\text{healthy cells}}$ (see Eq. 2) | 10000 |
| Screening factor in background, $\eta_{\text{background}}$ (see Eq. 2) | 10^6 |
| <i>Elasticity material properties</i> (see Hoge et al. 2007) | |
| Young's modulus of gray matter, E_{gm} (Pa) (see Eq. 3) | 2100 |
| Young's modulus of white matter, E_{wm} (Pa) (see Eq. 3) | 2100 |
| Young's modulus of cerebrospinal fluid, E_{csf} (Pa) (see Eq. 3) | 100 |
| Young's modulus of tumor, E_{tumor} (Pa) (see Eq. 3) | 2100 |
| Young's modulus of background material, E_{bcg} (Pa) (see Eq. 3) | 15000 |
| Poisson's ratio of gray matter, ν_{gm} (see Eq. 3) | 0.3 |
| Poisson's ratio of white matter, ν_{wm} (see Eq. 3) | 0.3 |
| Poisson's ratio of cerebrospinal fluid, ν_{csf} (see Eq. 3) | 0.1 |
| Poisson's ratio of background material, ν_{bcg} (see Eq. 3) | 0.48 |
| Poisson's ratio of tumor, ν_{tumor} (see Eq. 3) | 0.45 |
| Forcing function constant, ζ (see Eq. (11)) | 40000 |
| <i>Edema model parameters</i> | |
| Transmission rate of edematous fluid into extra-cellular space, δ_e (see Eq. 20) | 40 |
| Half-max invasive concentration, δ_{half} (see Eq. 20) | 0.01 |
| Drainage rate of edematous fluid, δ_l (see Eq. 20) | 80 |

For the screening parameters, we experiment with different values to obtain the best results (see Sect. 4.1 for other range of values that can be used and the sensitivity of the model to these values). For the edema model parameters, we refer to Hawkins-Daarud et al. (2013) and experiment with different values to produce the qualitative characteristics of edema in MRI images

- Solve the variable linear elasticity equation (Eq. 4c) using Krylov subspace methods with forcing function computed from c^{n+1} and Lamé coefficients computed from $(g^{n+1}, w^{n+1}, f^{n+1})$ to obtain \mathbf{u}^{n+1} . Update velocity \mathbf{u}_t^{n+1} using backward time differencing.

Now, we provide specific details of each step.

Solving the diffusion equation split For the diffusion equation, we use a pseudo-spectral spatial discretization with a Crank–Nicolson scheme in time. The diffusion equation reduces to:

$$\left(1 - \frac{\Delta t}{2} \mathcal{D}\right) c^{n+1} = \left(1 + \frac{\Delta t}{2} \mathcal{D}\right) c^n. \tag{22}$$

We solve this symmetric, implicit system of equations using the Conjugate Gradient (CG) method. We precondition this Krylov solver by solving the diffusion equation using constant coefficients computed by averaging the inhomogeneous diffusion coefficient over the spatial domain (similar to the works of Gholami et al. 2016).

Solving the transport equation splits All transport equations are solved using a semi-Lagrangian scheme, which is unconditionally stable for solving the linear advection equations. We use a second order in time and third order in space (for interpolation) to solve for the semi-Lagrangian trajectories of a scalar field, $v(\mathbf{x}, t)$. Here, we briefly describe the semi- Lagrangian scheme using the following transport equation:

$$\partial_t v + \nabla v \cdot \mathbf{u}_t = g(v, \mathbf{x}). \tag{23}$$

In this method, we compute a new grid point \mathbf{X} using the scheme below:

$$\mathbf{X}_* = \mathbf{x} - \Delta t \mathbf{u}_t(\mathbf{x}), \tag{24a}$$

$$\mathbf{X} = \mathbf{x} - \frac{\Delta t}{2} (\mathbf{u}_t(\mathbf{x}) + \mathbf{u}_t(\mathbf{X}_*)). \tag{24b}$$

We find the scalar field at the next time instant using:

$$v_*(\mathbf{x}) = v(\mathbf{X}, 0) + \Delta t g(v(\mathbf{X}, 0), X), \tag{25a}$$

$$g_*(\mathbf{x}) = g(v_*(\mathbf{x}), \mathbf{x}), \tag{25b}$$

$$v(\mathbf{x}, \Delta t) = v(\mathbf{X}, 0) + \frac{\Delta t}{2} (g(v(\mathbf{X}, 0), X) + g_*(\mathbf{x})). \tag{25c}$$

We use cubic interpolation to find field values at non-grid points \mathbf{X} and \mathbf{X}_* . Further details on the semi-Lagrangian method can be found in Mang et al. (2016).

Solving the variable elasticity equations To compute the displacement \mathbf{u} , we have to solve Eq. 4c. Since the Lamé coefficients are variable in the domain, we use the Generalized Minimum Residual Method (GMRES) to iteratively minimize the residual in the Krylov subspace of Eq. 4c, up to a user defined tolerance, τ . To increase the convergence rate, we precondition the variable elasticity equation by solving it with

constant Lamé coefficients computed by taking their average over the domain. The constant elasticity coefficient equation can be solved analytically as follows:

Using the identity of $\nabla \cdot (\nabla \mathbf{u} + \nabla \mathbf{u}^T) = \Delta \mathbf{u} + \nabla \nabla \cdot \mathbf{u}$, we need to solve the following equation:

$$\mathcal{L}\mathbf{u} = \mu \Delta \mathbf{u} + (\lambda + \mu) \nabla \nabla \cdot \mathbf{u} = \mathbf{b}. \tag{26}$$

Given the right hand side \mathbf{b} , we need to compute \mathbf{u} . Applying the Fourier transform on both sides, we obtain:

$$\left(\mu \boldsymbol{\omega}^T \boldsymbol{\omega} \mathbf{I} + (\lambda + \mu) \boldsymbol{\omega} \boldsymbol{\omega}^T \right) \widehat{\mathbf{u}} = \widehat{\mathbf{b}}, \tag{27}$$

where the hats denote the frequency domain, and $\boldsymbol{\omega}$ is the corresponding wave numbers. We, then, use the Sherman-Morrison formula to compute \mathbf{u} :

$$\mathbf{u} = \mathcal{F}^{-1} \left(\left(\frac{1}{\mu \boldsymbol{\omega}^T \boldsymbol{\omega}} - \frac{1}{(\mu \boldsymbol{\omega}^T \boldsymbol{\omega})^2} \frac{(\lambda + \mu) \boldsymbol{\omega} \boldsymbol{\omega}^T}{1 + \frac{\lambda + \mu}{\mu}} \right) \widehat{\mathbf{b}} \right), \tag{28}$$

where \mathcal{F}^{-1} is the inverse Fourier transform.

We enforce the zero tumor flux boundary condition and zero displacement boundary condition on the skull using appropriate smoothed penalized conditions using the penalty method (see Del Pino and Pironneau 2003; Hogeia et al. 2008 for more details).

For qualitative assessments of mass effect, we compute principal stresses and maximum shear stress at every time step, using the stress tensor calculated from Eq. 1a. The principal stresses are visualized by the trace of the stress tensor and the maximum shear stress is computed from the Mohr’s circle as:

$$\tau_{\max} = \sqrt{\frac{(\mathbf{T}_{xx} - \mathbf{T}_{yy})^2}{2} + \mathbf{T}_{xy}^2}, \tag{29}$$

where T is given in (1b). Further, for sensitivity of mass effect parameters like forcing factor ζ , we compute the determinant of the deformation gradient (also known as the Jacobian J) as follows:

$$\mathcal{J} = \det(I + \nabla u). \tag{30}$$

For the multispecies model, we solve all the equations in a similar fashion as the single species model. We employ the following operator splitting steps:

- Solve the advection equations $\partial_t q + \nabla \cdot (q \mathbf{u}_t) = 0$ for $q = (p, i, n, g, w)$ over time Δt using the semi-Lagrangian method with q^n as initial condition and current velocity \mathbf{u}_t^n to obtain $(p^\dagger, i^\dagger, n^\dagger, g^\dagger, w^\dagger)$.
- Solve the advection equation $\partial_t f + \nabla f \cdot \mathbf{u}_t = 0$ for f over time Δt using the semi-Lagrangian method with f^n as initial condition and current velocity \mathbf{u}_t^n to obtain f^{n+1} .

Table 4 Numerical parameters used in the forward simulations

| Parameter | Value |
|--|-------|
| Number of discretization points, $N_x = N_y = N_z$ | 256 |
| Time step, Δt | 0.01 |
| Tolerance for Krylov subspace solvers, τ | 0.001 |
| Time horizon | 1 |

- Solve the diffusion equations $\partial_t i - \mathcal{D}i = 0$ and $\partial_t o - \mathcal{D}o = 0$ over time Δt using the Crank-Nicolson method with i^\dagger and o^n as initial conditions to obtain $i^{\dagger\dagger}$ and o^\dagger .
- Solve the reaction equations $\partial_t q - \mathcal{R}_q = 0$ over time Δt explicitly with $(p^\dagger, i^{\dagger\dagger}, n^\dagger, g^\dagger, w^\dagger)$ as initial condition to obtain q^{n+1} . Here, \mathcal{R}_q is the reaction/source operator for Eqs. 12a–12e and 12j–12k. Update the reaction, diffusion and elasticity coefficients using the new healthy tissue and tumor concentration.
- Solve the reaction equation $\partial_t o + \mathcal{R}_o = 0$ over time Δt explicitly with o^\dagger as initial condition to obtain o^{n+1} .
- Solve the variable linear elasticity equation (Eq. 12i) using Krylov subspace methods with forcing function and Lamé coefficients computed from q^{n+1} to obtain \mathbf{u}^{n+1} . Update velocity \mathbf{u}_t^{n+1} using backward time differencing.

The numerical parameters used are highlighted in Table 4. The typical number of Krylov solves for the diffusion equation is around one to three Conjugate Gradient iterations. For the preconditioned linear elasticity equations, the number of GMRES iterations is typically around 50–60. Preconditioning with the constant elasticity operator is quite effective and enables us to reduce the number of Krylov iterations from over 1000 to about 50. Also note that the spectral preconditioner is very cheap to apply since it only involves fast Fourier transforms.

4 Numerical experiments

We perform a number of simulations to demonstrate qualitatively the behavior of our scheme, compare the single species with the multispecies model, illustrate the mass effect and the effects of screening, and explain how we can use our scheme to create synthetic MR images. In addition, we conduct a basic sensitivity analysis for a small number of parameters.

We perform all simulations using the BrainWeb atlas (Cocosco et al. 1997) (spatial resolution: 1 mm \times 1 mm \times 1 mm), which provides a realistic brain geometry segmented into gray matter, white matter and cerebrospinal fluid. We use these values as initial conditions for the evolution of material properties and cerebrospinal fluid. To visualize the results of our simulations, we segment the brain into material properties and tumor by choosing the label with maximum cell density at any voxel (Gooya et al. 2011). We overlay tumor concentrations onto these segmentations along with contours of the cerebrospinal fluid at $t = 0$ to observe the evolution of tumor cells and tumor-induced deformations in material properties.

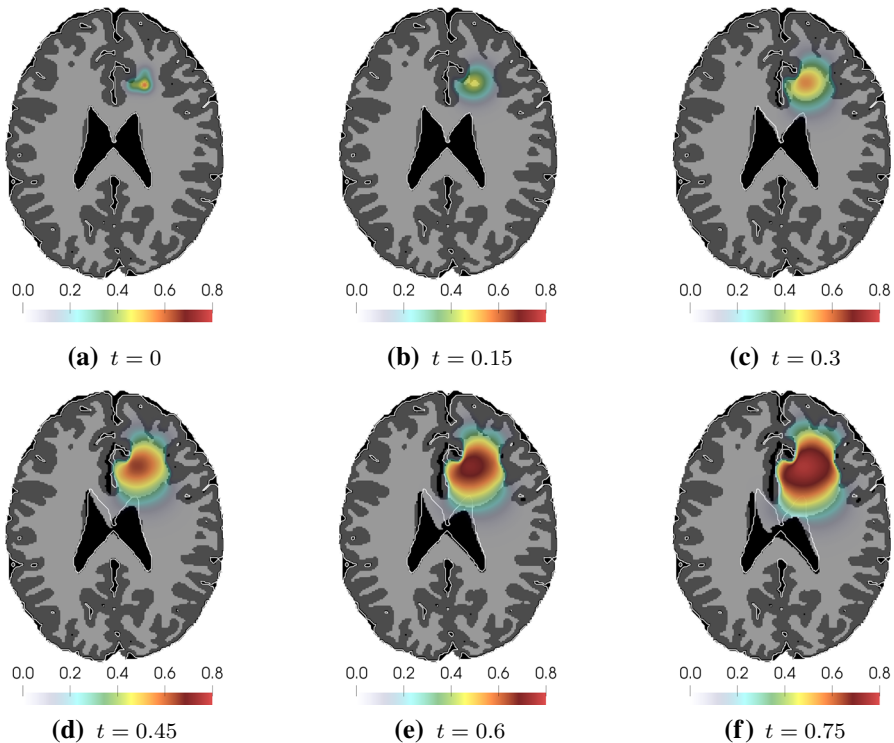


Fig. 3 Time evolution of segmentation of the brain and tumor concentration for the reaction–diffusion model with mass effect. The segmentations are overlaid with contours of the cerebrospinal fluid at initial time. As one can see, there is significant deformation of the cerebrospinal fluid and surrounding tissues

Single species mass effect We show an exemplary simulation for the single species model in Fig. 3. As we can see, there is a significant mass effect due to the growth of tumor on the surrounding tissues. The corresponding point-wise l_2 norm of the displacement fields are also highlighted in Fig. 4. Tissue deformation can be observed around the tumor boundary and it increases as the tumor grows and spreads. Specifically, we observe large displacements around the cerebrospinal fluid due to its soft and highly compressible nature.

Multispecies mass effect The results from the multispecies model with mass effect are shown in Fig. 5. The initial condition for proliferative cells is a Gaussian mixture and the invasive cells are taken as a small fraction of initial proliferative cell concentration. To better visualize the evolution of the different tumor cell types, we count all tumor phenotypes as one for the segmentation and overlay individual tumor concentrations.

We can see the characteristic multicomponent structure of a glioblastoma along with significant mass effect on the surrounding tissues in these simulations. This structure includes the necrotic tumor and tissue cells accumulating in a central core surrounded by an expanding rim of proliferating tumor cells. Regarding invasive tumor cells, recent histopathology reports (Eidel et al. 2017; Gill et al. 2014) show that they

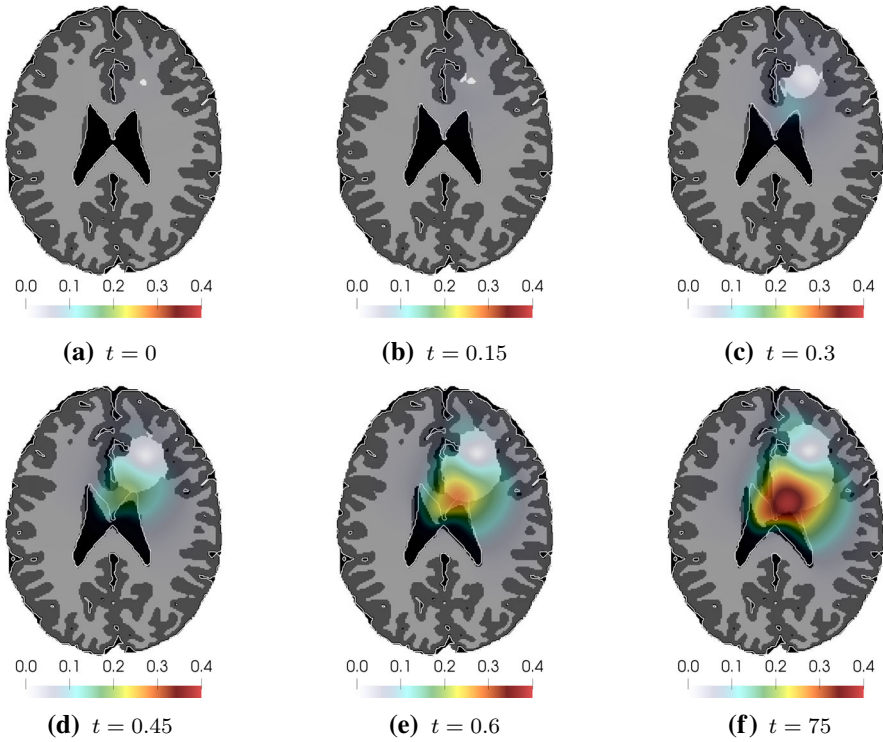


Fig. 4 Time evolution of the point-wise l_2 norm of the displacement field, u

infiltrate or diffuse to regions beyond the enhancing cancer rim. They also indicate that the invasive cell density is maximum in or around a central necrotic tumor region and becomes smaller as we move away from this region. We can observe these trends in invasive cell concentrations in our simulations. A 3D simulation of multispecies mass effect is shown in Fig. 6. The spatial discretization is equal in all directions.

Stress fields In order to visualize the stress fields, we show point-wise values for the principal stresses and maximum shear stress in Fig. 7. We outline how these are computed from the stress tensor in Eq. 29. The principal stress plot shows small tensile stresses induced in the tumor core and larger compressive stresses around the tumor boundary. The maximum shear stress is induced around the growing tumor region.

Screening effects We perform simulations for three different values of the screening coefficient outside the tumor ($\eta_{\text{healthy cells}}$) to observe its effects.

We visualize this in Fig. 8 using contours of cerebrospinal fluid to indicate the extent of its deformation for the three cases. A large value of $\eta_{\text{healthy cells}}$ indicates a highly localized mass effect to regions immediately around the tumor core. Smaller values result in observable mass effect in regions far away from the tumor core. However, for tumors close to the ventricles, a long-range mass effect can lead to their excessive shearing. Hence, a reasonable screening parameter is helpful for capturing realistic deformations.

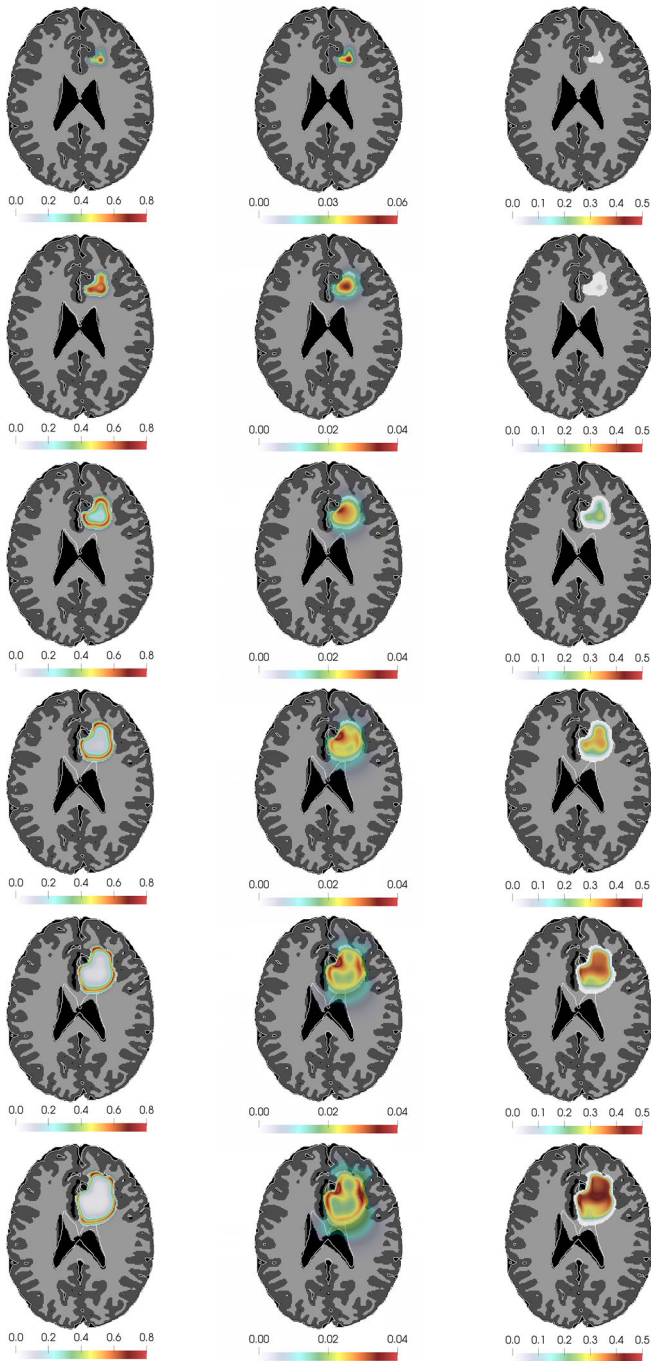


Fig. 5 Time evolution of proliferative (column 1), infiltrative (column 2), necrotic (column 3) tumor cell concentrations. The concentrations are overlaid on the whole tumor core segmentation (proliferative and necrotic tumor). The rows show different time instances of the simulation: $t = 0, 0.2, 0.4, 0.6, 0.8, 1.0$

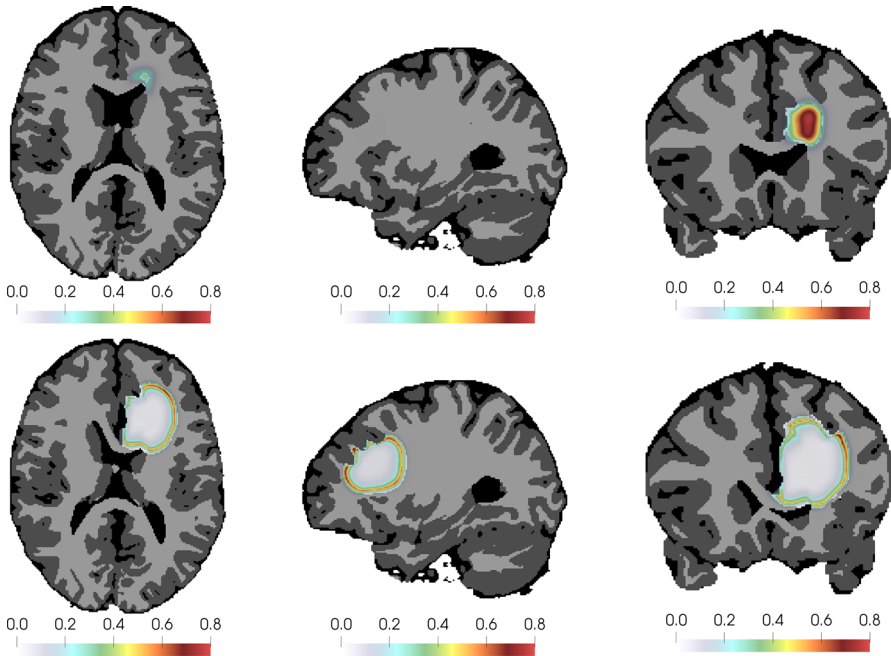


Fig. 6 Segmented images of 3D simulation showing the evolution of proliferating cells using the multi-species mass effect model at $t = 0$ (top row) and $t = 1$ (bottom row) for axial slice 123, sagittal slice 97 and coronal slice 166

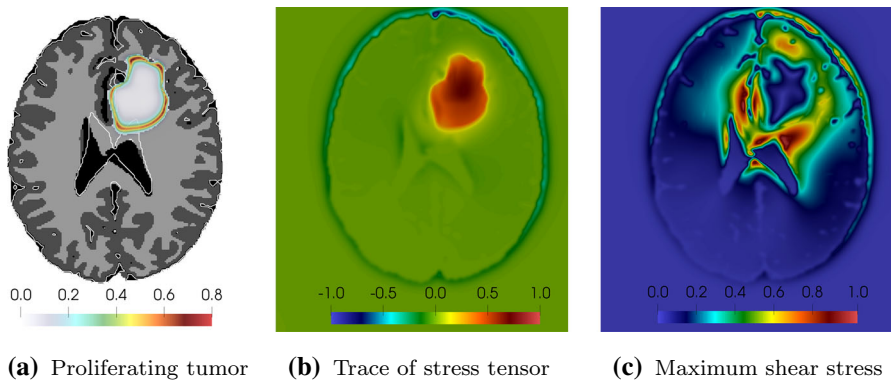


Fig. 7 Normalized stress plots for single species mass effect at $t = 1$

Simulated MRI images We use the segmentation for tumor cells and healthy cells to simulate MRI images by sampling intensities from real MRI scans. The segmentation of the brain is obtained by assigning every voxel to the species label with maximum concentration. We define the map from the segmentation to the simulated MRI as follows:

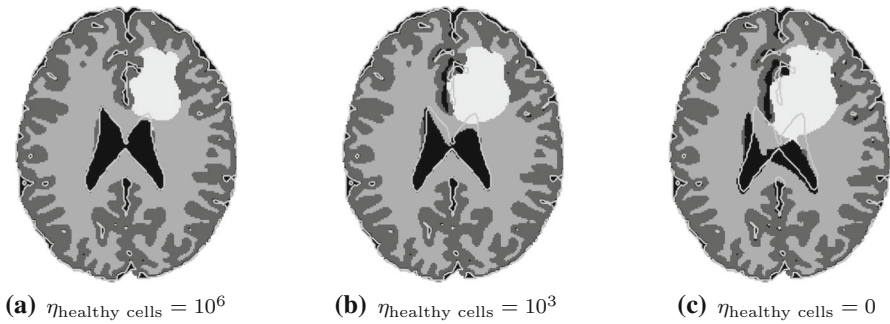


Fig. 8 Effect of screening coefficient, $\eta_{\text{healthy cells}}$ on cerebrospinal fluid deformation. The cerebrospinal fluid contours are overlaid on the initial segmentation for three screening coefficients

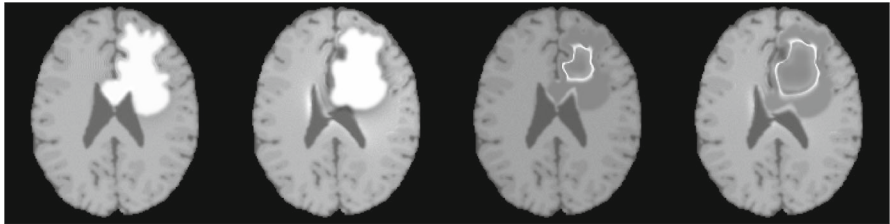


Fig. 9 Simulated T1-Gd MRI images: (left to right) Single species model with and without mass effect, multispecies model with and without mass effect. The intensities for the tumor cells in the single species model are sampled from enhancing tumor structures of real MRI scans

$$\psi_{\text{sim}}(\mathbf{x}) = \sum_{\iota} c^{\iota}(\mathbf{x}) \psi_{\text{MRI}}^{\iota}, \quad (31)$$

where $\psi_{\text{sim}}(\mathbf{x})$ is the intensity of the simulated MRI scan, $c^{\iota}(\mathbf{x})$ is a smoothed probability map of species ι obtained from the segmentation and $\psi_{\text{MRI}}^{\iota}$ is the sampled intensity from a real MRI scan for species ι . We sample real intensities by taking the mean intensity of the corresponding species in the real MRI modality we wish to simulate. We also randomly perturb this intensity within 10% of its standard deviation to introduce noise. We use a few brains from the GLISTR dataset (Gooya et al. 2012) which contain the ground truth segmentation to find the mean intensity and its standard deviation for each species and MRI modality.

We compare simulated T1-Gd MRI images from the different models in Fig. 9. Unlike the multispecies model, the single species model provides no information about the enhancing and necrotic tumor structures. It also does not show edema which can be correlated with the extent of infiltration by tumor cells. Further, without mass effect, neither of the models capture realistic deformations of the ventricles and other tissue types. More exemplar simulated MRI scans are shown in Fig. 10, with varying initial conditions for the tumor location.

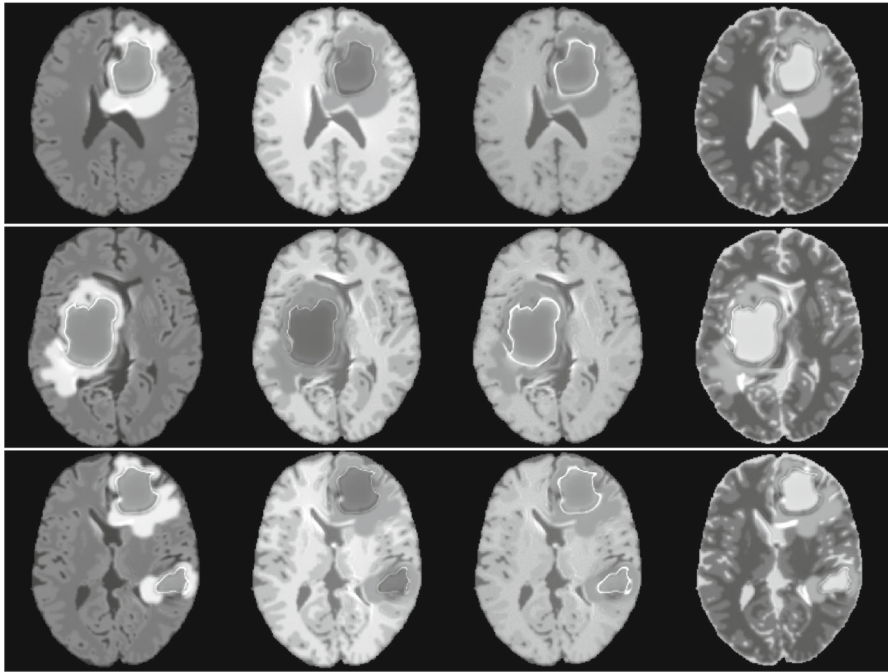


Fig. 10 Simulated MRI images (FLAIR, T1, T1-Gd and T2) of tumors with different initial conditions. The bottom row shows a multi-focal tumor growth simulation. The hyper-intense regions of the FLAIR images show the extent of edematous fluid and the delineated enhancing and necrotic tumor structures can be seen from the T1-Gd images. All tumors produce significant mass effect on the surrounding brain tissue

4.1 Sensitivity analysis

We perform a sensitivity analysis to find which parameters in the model are most sensitive. To determine the effects of the parameters in the multispecies model, we calculate their respective gradients using finite differences, by varying one factor at a time:

$$g_{\iota} = \frac{\|\iota\| - \|\iota^*\|}{\epsilon \|\iota^*\|}, \quad (32)$$

where ι is the tumor species concentration, ι^* is an “optimal” species concentration (obtained using the parameters from Table 3) and ϵ is a small perturbation to the parameter in consideration. We assess the sensitivity of each tumor species to the different parameters by comparing their respective gradients g_{ι} . The results are shown in Table 5. Proliferative cell concentrations are most sensitive to the oxygen hypoxia threshold (ρ_{hypoxia}) and the reaction coefficient (ρ). While the reaction coefficient controls the proliferative rate, the hypoxia threshold has strong influence on the conditions which lead to phenotype switching and necrosis. Other oxygen parameters such as the oxygen consumption (δ_{ρ}) also affect the concentration, but not as strongly. Invasive cell concentrations are most sensitive to the transition rate from proliferative to invasive

Table 5 Sensitivity of the multispecies tumor model on different model parameters evaluated through gradients computed by varying one factor at a time

| Parameter | g_p | g_i | g_n |
|---|--------|--------|--------|
| Reaction coefficient, ρ (see Eq. 10) | 0.377 | 1.798 | 0.687 |
| Hypoxia threshold, ρ_{hypoxia} (see Eq. 14) | -0.532 | -0.124 | 0.369 |
| Deathrate, γ (see Eq. 14) | -0.166 | -0.123 | 0.710 |
| Transition rate from p to i , α_0 (see Eq. 17) | -0.029 | 0.304 | 0 |
| Oxygen consumption, δ_p (see Eq. 12g) | -0.240 | -0.096 | 0.247 |
| Oxygen source, δ_s (see Eq. 12g) | 0.15 | 0.059 | -0.146 |
| Transition rate from i to p , β_0 (see Eq. 18) | 0.003 | -0.012 | 0 |
| Diffusion coefficient, k (see Eq. 8) | 0.065 | -0.026 | -0.042 |

cells (α_0) and the reaction coefficient since these parameters contribute to the source of invasive cells. Necrotic cells are affected largely by the death rate (γ), hypoxia threshold and reaction coefficient. None of the tumor concentrations are sensitive to the transition rate from invasive to proliferative cells (β_0). The solution doesn't seem to be very sensitive to the diffusion coefficient (k) at least for the range of parameters we tested. These results show a consistent importance of the reaction coefficient and hypoxia threshold for all tumor species. But, the effect of other parameters is variable amongst the different species.

To assess the sensitivity of the model to mass effect, we perform a grid-search on two parameters: screening coefficient of healthy cells, $\eta_{\text{healthy cells}}$ and forcing function constant, ζ . We report the L2 norm of the Jacobian (determinant of the deformation gradient, see Eq. 30), \mathcal{J} and the maximum distance of a displacement contour (corresponding to a displacement of 0.1 voxels) from the initial tumor seed, d_{max} . This threshold was chosen to visualize the localization effects of the screening coefficient.

Figure 11 shows that the deformation Jacobian increases with higher forcing factors and smaller screening, which is unsurprising. The localization effect of the screening coefficient is captured in Fig. 12. This results provides us with information regarding the range of screening coefficients and forcing factors that would be useful to capture realistic deformations.

4.2 Mesh convergence

We perform a simple mesh convergence study. We discretize uniformly in all directions using mesh size $h = 2\pi/512$ as the ground truth/reference and report the error measure e_i for species i , defined as:

$$e_i = \frac{\|\iota_h - \iota_{\text{ref}}\|_2}{\|\iota_{\text{ref}}\|_2}, \quad (33)$$

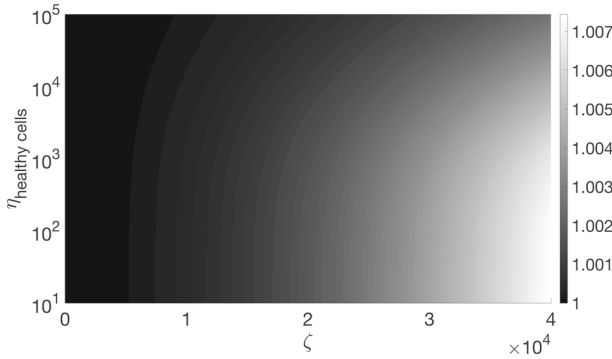


Fig. 11 Plot of the L2 norm of the re-scaled deformation Jacobian \mathcal{J} (see Eq. 30). The L2 norm of the Jacobian is large for higher forcing factors ζ and lower screening coefficients $\eta_{\text{healthy cells}}$. High ζ values means large body forces and hence larger Jacobians. With smaller screening coefficients, the range mass effect is longer resulting in larger Jacobians

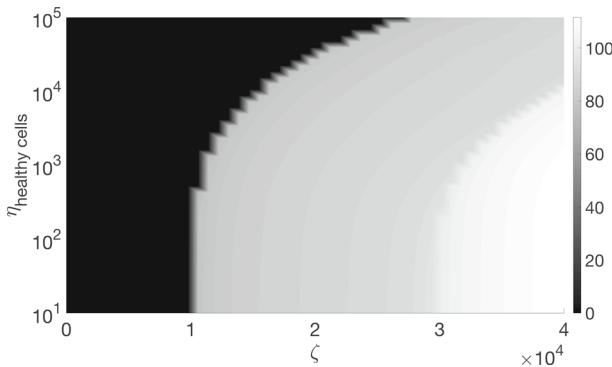


Fig. 12 Plot of displacement metric, d_{max} . We calculate this for any $(\eta_{\text{healthy cells}}, \zeta)$ by finding the displacement contour corresponding to 0.1 voxels and computing the maximum distance of this contour from the location of the initial tumor seed (which is fixed). Given an understanding of how large deformations are typically in glioblastoma growth, this figure shows us how specific ranges of $(\eta_{\text{healthy cells}}, \zeta)$ can be more useful in obtaining a realistic tissue displacement

Table 6 L_2 convergence error rates e_l for different model species. The table shows an approximate linear convergence rate as expected for our numerical methods

| Mesh size, h | e_p | e_i | e_n | e_g | e_w |
|----------------|--------|--------|--------|--------|--------|
| $2\pi/64$ | 0.5677 | 0.1904 | 0.1677 | 0.2984 | 0.2421 |
| $2\pi/128$ | 0.3437 | 0.1483 | 0.0986 | 0.1379 | 0.1171 |
| $2\pi/256$ | 0.1510 | 0.0645 | 0.0382 | 0.0291 | 0.0292 |

where t_h is the concentration of species t at any mesh size h and t_{ref} is the reference concentration of species t . We refine both space and time together to observe our numerical convergence rate. We report our results in Table 6. We can observe an approximate first order of convergence for our numerical schemes, as expected.

5 Conclusions and future work

We presented a model that captures the phenomenological features of glioblastomas seen on MRI scans. These features include a multicomponent structure of a glioblastoma and tumor-induced mass effect on surrounding brain tissue. We coupled a multispecies “go-or-grow” tumor model with linear elasticity equations and presented results to illustrate the capabilities of our model in capturing different tumor characteristics using novel numerical schemes. We are currently working on extending the sensitivity analysis and understanding the important parameters of the model by formulating an inverse problem and directly inverting for parameters from images using adjoint-based gradient methods.

References

- Akbari H, Macyszyn L, Da X, Bilello M, Wolf RL, Martinez-Lage M, Biros G, Alonso-Basanta M, O'Rourke DM, Davatzikos C (2016) Imaging surrogates of infiltration obtained via multiparametric imaging pattern analysis predict subsequent location of recurrence of glioblastoma. *Neurosurgery* 78(4):572–580
- Alarcón T, Byrne H, Maini P (2003) A cellular automaton model for tumour growth in inhomogeneous environment. *J Theor Biol* 225(2):257–274
- Anderson ARA, Rejniak KA, Gerlee P, Quaranta V (2009) Microenvironment driven invasion: a multiscale multimodel investigation. *J Math Biol* 58(4–5):579–624
- Bakas S, Akbari H, Sotiras A, Bilello M, Rozycki M, Kirby J, Freymann J, Farahani K, Davatzikos C (2017a) Segmentation labels for the pre-operative scans of the TCGA-GBM collection. *Cancer Imaging Arch*. <https://doi.org/10.7937/K9/TCIA.2017.KLXWJJ1Q>
- Bakas S, Akbari H, Sotiras A, Bilello M, Rozycki M, Kirby JS, Freymann JB, Farahani K, Davatzikos C (2017b) Advancing the cancer genome atlas glioma MRI collections with expert segmentation labels and radiomic features. *Sci Data* 4:170117
- Bellomo N, Li N, Maini PK (2008) On the foundations of cancer modelling: selected topics, speculations, and perspectives. *Math Models Methods Appl Sci* 18(04):593–646
- Clatz O, Sermesant M, Bondiau P-Y, Delingette H, Warfield SK, Malandain G, Ayache N (2005) Realistic simulation of the 3-d growth of brain tumors in MR images coupling diffusion with biomechanical deformation. *IEEE Trans Med Imaging* 24(10):1334–1346
- Cocosco CA, Kollokian V, Kwan RK-S, Pike GB, Evans AC (1997) Brainweb: Online interface to a 3d MRI simulated brain database. In: *NeuroImage*. Citeseer
- Crank J, Nicolson P (1996) A practical method for numerical evaluation of solutions of partial differential equations of the heat-conduction type. *Adv Comput Math* 6(1):207–226
- Del Pino S, Pironneau O (2003) A fictitious domain based general PDE solver. In: Kuznetsov Y, Neitanmaki P, Pironneau O (eds) *Numerical methods for scientific computing variational problems and applications*. CIMNE, Barcelona
- Dolecek TA, Propp JM, Stroup NE, Kruchko C (2012) CBTRUS statistical report: primary brain and central nervous system tumors diagnosed in the United States in 2005–2009. *Neuro-oncology* 14(suppl 5):v1–v49
- Eidel O, Burth S, Neumann J-O, Kieslich PJ, Sahn F et al (2017) Tumor infiltration in enhancing and non-enhancing parts of glioblastoma: a correlation with histopathology. *PLoS ONE* 12(1):e0169292
- Falcone M, Ferretti R (1998) Convergence analysis for a class of high-order semi-Lagrangian advection schemes. *SIAM J Numer Anal* 35(3):909–940
- Gerlee P, Anderson A (2009) Evolution of cell motility in an individual-based model of tumour growth. *J Theor Biol* 259(1):67–83
- Gholami A, Mang A, Biros G (2016) An inverse problem formulation for parameter estimation of a reaction–diffusion model of low grade gliomas. *J Math Biol* 72(1):409–433

- Gholami A, Subramanian S, Shenoy V, Himthani N, Yue X, Zhao S, Jin P, Biros G, Keutzer K (2018) A novel domain adaptation framework for medical image segmentation. In: The multimodal brain tumor image segmentation benchmark (BRATS), MICCAI
- Giese A, Kluwe L, Laube B, Meissner H, Berens ME, Westphal M (1996) Migration of human glioma cells on myelin. *Neurosurgery* 38(4):755–764
- Giese A, Bjerkvig R, Berens M, Westphal M (2003) Cost of migration: invasion of malignant gliomas and implications for treatment. *J Clin Oncol* 21(8):1624–1636
- Gill BJ, Pisapia DJ, Malone HR, Goldstein H, Lei L, Sonabend A, Yun J, Samanamud J, Sims JS, Banu M, Dovas A, Teich AF, Sheth SA, McKhann GM, Sisti MB, Bruce JN, Sims PA, Canoll P (2014) MRI-localized biopsies reveal subtype-specific differences in molecular and cellular composition at the margins of glioblastoma. *Proc Natl Acad Sci* 111(34):12550–12555
- Gooya A, Biros G, Davatzikos C (2011) Deformable registration of glioma images using EM algorithm and diffusion reaction modeling. *IEEE Trans Med Imaging* 30(2):375–390
- Gooya A, Pohl K, Bilello M, Cirillo L, Biros G, Melhem E, Davatzikos C (2012) GLISTR: Glioma image segmentation and registration. *IEEE Trans Med Imaging* PP(99):1
- Goriely A, Moulton DE (2011) The physics and mechanics of biological systems. In: New trends in the physics and mechanics of biological systems: lecture notes of the Les Houches Summer Schools, vol 92. <https://doi.org/10.1093/acprof:oso/9780199605835.001.0001>
- Hatzikirou H, Basanta D, Simon M, Schaller K, Deutsch A (2012) ‘go or grow’: the key to the emergence of invasion in tumour progression? *Math Med Biol J IMA* 29(1):49–65
- Hawkins-Daarud A, Rockne RC, Anderson ARA, Swanson KR (2013) Modeling tumor-associated edema in gliomas during anti-angiogenic therapy and its impact on imageable tumor. *Front Oncol* 3:66
- Hogea C, Abraham F, Biros G, Davatzikos C (2006) A framework for soft tissue simulations with applications to modeling brain tumor mass-effect in 3D images. In: Medical image computing and computer-assisted intervention workshop on biomechanics, Copenhagen
- Hogea C, Davatzikos C, Biros G (2007) Modeling glioma growth and mass effect in 3D MR images of the brain. In: *Lect Notes Comput Sc*, vol 4791, pp 642–650
- Hogea C, Davatzikos C, Biros G (2008) An image-driven parameter estimation problem for a reaction–diffusion glioma growth model with mass effect. *J Math Biol* 56:793–825
- Hormuth DA, Eldridge SL, Weis JA, Miga MI, Yankeelov TE (2018) Mechanically coupled reaction–diffusion model to predict glioma growth: methodological details. *Methods Mol Biol* 1711:225–241
- Jbabdi S, Mandonnet E, Duffau H, Capelle L, Swanson KR, Pélégriani-Issac M, Guillevin R, Benali H (2005) Simulation of anisotropic growth of low-grade gliomas using diffusion tensor imaging. *Magn Reson Med* 54(3):616–624
- Konukoglu E, Clatz O, Boudiau P-Y, Delingette H, Ayache N (2010a) Extrapolating glioma invasion margin in brain magnetic resonance images: suggesting new irradiation margins. *Med Image Anal* 14(2):111–125
- Konukoglu E, Clatz O, Menze BH, Stieltjes B, Weber M-A, Mandonnet E, Delingette H, Ayache N (2010b) Image guided personalization of reaction–diffusion type tumor growth models using modified anisotropic Eikonal equations. *IEEE Trans Med Imaging* 29(1):77–95
- Macyszyn L, Akbari H, Pisapia JM, Da X, Attiah M, Pigrish V, Bi Y, Pal S, Davuluri RV, Roccograndi L, Dahmane N, Martinez-Lage M, Biros G, Wolf RL, Bilello M, O’Rourke DM, Davatzikos C (2016) Imaging patterns predict patient survival and molecular subtype in glioblastoma via machine learning techniques. *Neuro-Oncology* 18(3):417–425
- Mang A, Toma A, Schuetz TA, Becker S, Eckey T, Mohr C, Petersen D, Buzug TM (2012) Biophysical modeling of brain tumor progression: from unconditionally stable explicit time integration to an inverse problem with parabolic PDE constraints for model calibration. *Med Phys* 39(7):4444–4459
- Mang A, Gholami A, Biros G (2016) Distributed-memory large-deformation diffeomorphic 3D image registration. In: Proc ACM/IEEE conference on supercomputing
- Menze BH, Jakab A, Bauer S, Kalpathy-Cramer J, Farahani K, Kirby J, Burren Y, Porz N, Slotboom J, Wiest R et al (2015) The multimodal brain tumor image segmentation benchmark (brats). *IEEE Trans Med Imaging* 34(10):1993–2024
- Mohamed A, Davatzikos C (2005) Finite element modeling of brain tumor mass-effect from 3d medical images. In: Medical image computing and computer-assisted intervention–MICCAI 2005. Springer, pp 400–408
- Oden JT, Prudencio EE, Hawkins-Daarud A (2013) Selection and assessment of phenomenological models of tumor growth. *Math Models Methods Appl Sci* 23(07):1309–1338

- Painter K, Hillen T (2013) Mathematical modelling of glioma growth: the use of diffusion tensor imaging (DTI) data to predict the anisotropic pathways of cancer invasion. *J Theor Biol* 323:25–39
- Pham K, Chauviere A, Hatzikirou H, Li X, Byrne HM, Cristini V, Lowengrub J (2012) Density-dependent quiescence in glioma invasion: instability in a simple reaction-diffusion model for the migration/proliferation dichotomy. *J Biol Dyn* 6(sup1):54–71
- Rahman MM, Feng Y, Yankeelov TE, Oden JT (2017) A fully coupled space-time multiscale modeling framework for predicting tumor growth. *Comput Methods Appl Mech Eng* 320:261–286
- Rekik I, Allassonnière S, Clatz O, Geremia E, Stretton E, Delingette H, Ayache N (2013) Tumor growth parameters estimation and source localization from a unique time point: application to low-grade gliomas. *Comput Vis Image Underst* 117(3):238–249
- Saut O, Lagaert J-B, Colin T, Fathallah-Shaykh HM (2014) A multilayer grow-or-go model for GBM: effects of invasive cells and anti-angiogenesis on growth. *Bull Math Biol* 76(9):2306–2333
- Strang G (1968) On the construction and comparison of difference schemes. *SIAM J Numer Anal* 5(3):506–517
- Stupp R, Mason WP, van den Bent MJ, Weller M, Fisher B, Taphoorn MJ, Belanger K, Brandes AA, Marosi C, Bogdahn U, Curschmann J, Janzer RC, Ludwin SK, Gorlia T, Allgeier A, Lacombe D, Cairncross JG, Eisenhauer E, Mirimanoff RO (2005) Radiotherapy plus concomitant and adjuvant temozolomide for glioblastoma. *N Engl J Med* 352(10):987–996
- Swan A, Hillen T, Bowman JC, Murtha AD (2018) A patient-specific anisotropic diffusion model for brain tumour spread. *Bull Math Biol* 80(5):1259–1291
- Swanson KR (2008) Quantifying glioma cell growth and invasion in vitro. *Math Comput Model* 47(5):638–648
- Swanson K, Alvord E, Murray J (2000) A quantitative model for differential motility of gliomas in grey and white matter. *Cell Prolif* 33(5):317–330
- Swanson KR, Alvord E, Murray J (2002) Virtual brain tumours (gliomas) enhance the reality of medical imaging and highlight inadequacies of current therapy. *Br J Cancer* 86(1):14–18
- Swanson KR, Rockne RC, Claridge J, Chaplain MA, Alvord EC, Anderson AR (2011) Quantifying the role of angiogenesis in malignant progression of gliomas: in silico modeling integrates imaging and histology. *Cancer Res* 71(24):7366–7375
- Szeto MD, Chakraborty G, Hadley J, Rockne R, Muzi M, Alvord EC, Krohn KA, Spence AM, Swanson KR (2009) Quantitative metrics of net proliferation and invasion link biological aggressiveness assessed by MRI with hypoxia assessed by FMISO-PET in newly diagnosed glioblastomas. *Cancer Res* 69(10):4502–4509
- Yankeelov TE, Atuegwu N, Hormuth D, Weis JA, Barnes SL, Miga MI, Rericha EC, Quaranta V (2013) Clinically relevant modeling of tumor growth and treatment response. *Sci Transl Med* 5(187):187ps9